

Dalton Transactions

Accepted Manuscript



This is an *Accepted Manuscript*, which has been through the Royal Society of Chemistry peer review process and has been accepted for publication.

Accepted Manuscripts are published online shortly after acceptance, before technical editing, formatting and proof reading. Using this free service, authors can make their results available to the community, in citable form, before we publish the edited article. We will replace this *Accepted Manuscript* with the edited and formatted *Advance Article* as soon as it is available.

You can find more information about *Accepted Manuscripts* in the [Information for Authors](#).

Please note that technical editing may introduce minor changes to the text and/or graphics, which may alter content. The journal's standard [Terms & Conditions](#) and the [Ethical guidelines](#) still apply. In no event shall the Royal Society of Chemistry be held responsible for any errors or omissions in this *Accepted Manuscript* or any consequences arising from the use of any information it contains.

Cite this: DOI: 10.1039/c0xx00000x

www.rsc.org/xxxxxx

ARTICLE TYPE

Nanometer-Scale Separation of d^{10} Zn^{2+} -Layers and Twin-Shift Competition in $\text{Ba}_8\text{ZnNb}_6\text{O}_{24}$ -Based 8-Layer Hexagonal Perovskites

Fengqi Lu,^a Xiaoming Wang,^b Zhengwei Pan,^c Fengjuan Pan,^c Shiqiang Chai,^c Chaolun Liang,^d Quanchao Wang,^a Jing Wang,^c Liang Fang,^a Xiaojun Kuang^{a,c,*} and Xiping Jing^{b,*}⁵ Received (in XXX, XXX) Xth XXXXXXXXXX 20XX, Accepted Xth XXXXXXXXXX 20XX

DOI: 10.1039/b000000x

8-layer shifted hexagonal perovskite compound $\text{Ba}_8\text{ZnNb}_6\text{O}_{24}$ was isolated via controlling the ZnO volatilization, which features long-range B-cation ordering with nanometer-scale separation by ~ 1.9 nm of octahedral d^{10} cationic (Zn^{2+}) layers within the purely corner-sharing octahedral d^0 cationic (Nb^{5+}) host. The long-range ordering of B-site vacancy and out-of-center distortion of the highly-charged d^0 Nb^{5+} that is assisted by the second-order Jahn-Teller effect contribute to this unusual B-cation ordering in $\text{Ba}_8\text{ZnNb}_6\text{O}_{24}$. Small amount ($\sim 15\%$) of d^{10} Sb^{5+} substitutions for Nb^{5+} in $\text{Ba}_8\text{ZnNb}_{6-x}\text{Sb}_x\text{O}_{24}$ dramatically transformed the shifted structure to a twinned structure, in contrast with the $\text{Ba}_8\text{ZnNb}_{6-x}\text{Ta}_x\text{O}_{24}$ case requiring 50% d^0 Ta^{5+} substitution for Nb^{5+} for such shift-to-twin transformation. Multiple factors including B-cationic sizes, electrostatic repulsion force, long-range ordering of B-site vacancies, and bonding preferences arising from covalent contribution to B-O bonding that includes out-of-center octahedral distortion and B-O-B bonding angle could subtly contribute to the twin-shift phase competition of B-site deficient 8-layer hexagonal perovskites $\text{Ba}_8\text{B}_7\text{O}_{24}$. The ceramics of new shifted $\text{Ba}_8\text{ZnNb}_6\text{O}_{24}$ and twinned $\text{Ba}_8\text{ZnNb}_{5.1}\text{Sb}_{0.9}\text{O}_{24}$ compounds exhibited good microwave dielectric properties ($\epsilon_r \sim 35$, $Q_f \sim 36200 - 43400$ GHz and $\tau_f \sim 38 - 44$ ppm/ $^\circ\text{C}$).

Introduction

Cation order-disorder in ABO_3 perovskite structures¹ and its derivatives is important as it plays key role on controlling their crystal chemistry and physical properties such as the magnetism,² dielectric properties,^{1,3,4} ionic mobility.⁵ Cation ordering may be driven by the differences of charge, sizes and bonding preferences between the cations.^{4,6} The most common cation-ordering in perovskites occurs on the B-sites; the classical B-site ordering takes place along $\langle 111 \rangle$ stacking direction of the close packed AO_3 layers, forming 1:1-ordered double and 2:1-ordered complex perovskites with 6-layer and 3-layer repeats of octahedral networks along the stacking direction of AO_3 layers, respectively.^{4,7} Long-range cation ordering, which offers the possibility for assembly of different components at the nanometer scale for desired functions, is a significant challenge to the synthetic chemists.^{8,9} The periodically spontaneous phase separation at nanometer scale reported recently in perovskites, including $\text{Nd}_{2/3-x}\text{Li}_{3x}\text{TiO}_3$,⁹ NaLaMgWO_6 ,¹⁰ and $\text{NaNb}_{1-x}\text{Ta}_x\text{O}_3$ ¹¹ represents special nanometer-scale cation ordering arising from complex, compositionally-modulated structures. Understanding the interplay between the various chemical factors and the cation ordering is essential before producing the long-range ordering at nanometer scale of cations or cationic-anionic aggregates in a controllable and natural manner.

⁴⁵ 2:1-ordered complex perovskite received considerable

attention in the field of dielectric materials.^{3,6} As the examples, $\text{Ba}_3\text{MgTa}_2\text{O}_9$ and $\text{Ba}_3\text{ZnTa}_2\text{O}_9$ tantalates possess superior Q_f values $\sim 150\,000 - 250\,000$ GHz and near zero coefficient of resonant frequency τ_f , rendering them excellent resonators and filters for mobile network.³ These complex perovskite tantalates suffer from prolonged high-temperature processing required for densification as well as the B-cation ordering to achieve high Q_f values.¹² Additionally, the high cost of Ta_2O_5 raw material could hinder their continuous industrial production. All of these stimulated the search for cheaper niobate substitutes.¹³ Although the cation order kinetics in niobates is more sluggish than that in tantalates, some niobate complex perovskites were found to possess high Q_f values $\sim 100\,000$ GHz comparable to the tantalates e.g. $\text{Ba}_3(\text{Zn}_{1-x}\text{Co}_x)\text{Nb}_2\text{O}_9$ -based materials.^{13,14} The slightly cationic deficiency was found to effectively improve the cation ordering in complex perovskites.^{15,16} For example, in $\text{Ba}_3\text{ZnTa}_2\text{O}_9$ dielectric resonators,¹⁵ the ZnO volatility at high-temperature processing is an important factor on controlling the B-cation ordering and phase formation thus affecting the microwave dielectric properties. The B-cation deficient hexagonal perovskite phase $\text{Ba}_8\text{ZnTa}_6\text{O}_{24}$ ¹⁷ was usually observed as a minor impurity in $\text{Ba}_3\text{ZnTa}_2\text{O}_9$, which appeared not to deteriorate the quality factor of $\text{Ba}_3\text{ZnTa}_2\text{O}_9$ resonators. The isolation and characterization of $\text{Ba}_8\text{ZnTa}_6\text{O}_{24}$ resonators by Rosseinsky *et al*¹⁸ and Davies *et al*¹⁷ revealed that it adopts partially vacancy-ordered 8-layer twinned hexagonal perovskite structure (Figure 1a) with high Q_f values $\sim 68\,000 - 79\,000$ GHz,

except for its relatively large τ_f values $\sim 30 - 40$ ppm/ $^{\circ}\text{C}$. Similar to the complex perovskites, the ordering of cations and vacancy in face-sharing octahedral (FSO) B-sites of the B-site deficient twinned hexagonal structure improve the quality factor¹⁹ and such cation and vacancy ordering in the twinned structure occurs naturally, unlike the thermally-activated B-site cation-ordering in complex perovskites requiring prolonged heating. This stimulated successive exploitation on the B-site deficient hexagonal perovskites, which led to a series of high-Q 8-layer twinned hexagonal perovskite resonators including $\text{Ba}_8\text{MTa}_6\text{O}_{24}$ ($\text{M} = \text{Zn}^{17}, \text{Ni}^{20}, \text{Co}^{20}$), $\text{Ba}_8\text{Ga}_{4-x}\text{Ta}_{4+0.6x}\text{O}_{24}$ ²¹ as well as the B-site fully-occupied $\text{Ba}_8\text{Li}_2\text{Ta}_6\text{O}_{24}$.^{22, 23}

The search for the 8-layer twinned hexagonal perovskite niobates found less stability for the niobates than the tantalates. For example, Mallinson *et al*⁸ found that $\text{Ba}_8\text{ZnNb}_6\text{O}_{24}$ formed a mixed $\text{Ba}_5\text{Nb}_4\text{O}_{15}$ and $\text{Ba}_3\text{ZnNb}_2\text{O}_9$ phases although Freer *et al*²⁴ and Solomon *et al*²⁵ made $\text{Ba}_8\text{ZnNb}_6\text{O}_{24}$ and claimed that it is isostructural with the twinned $\text{Ba}_8\text{ZnTa}_6\text{O}_{24}$. Apart from the instability, the niobates display twin-shift competition, in contrast with the Ta-compositions displaying a strong preference for the

twinned structure. The twinned and shifted structures (Figure 1) consist of cubic (*c*) and hexagonal (*h*) BaO_3 layers stacked according to sequences of $(ccch)_2$ and $ccccchh$, respectively. Among the reported 8-layer hexagonal perovskite niobates, $\text{Ba}_8\text{Li}_2\text{Nb}_6\text{O}_{24}$ ²² adopts a twinned structure with a simple 8-layer hexagonal perovskite cell (Figure 1b); $\text{Ba}_8\text{Ti}_3\text{Nb}_4\text{O}_{24}$,²⁶ which is isostructural with twinned $\text{Ba}_8\text{ZnTa}_6\text{O}_{24}$, adopts an expanded cell by $\sqrt{3}$ in the *ab* plane of the simple 8-layer hexagonal perovskite cell (Figure 1a); while $\text{Ba}_8\text{CoNb}_6\text{O}_{24}$ adopts a shifted structure (Figure 1c). The hexagonal stacking of AO_3 layer introduces the FSO sites, which are able to accommodate the B-site vacancies. In the 8-layer B-site deficient hexagonal perovskites, B-site vacancies display either partial ordering in the FSO dimers in the twinned structure (Figure 1a) or completely long-range ordering between two consecutive hexagonal layers in the shifted structure, forming single empty octahedral layers in the central position of the FSO trimers (Figure 1c). The key factors controlling the twin-shift option for the 8-layer hexagonal perovskite niobates and tantalates and the long-range cation ordering in the shifted structure are not well understood.

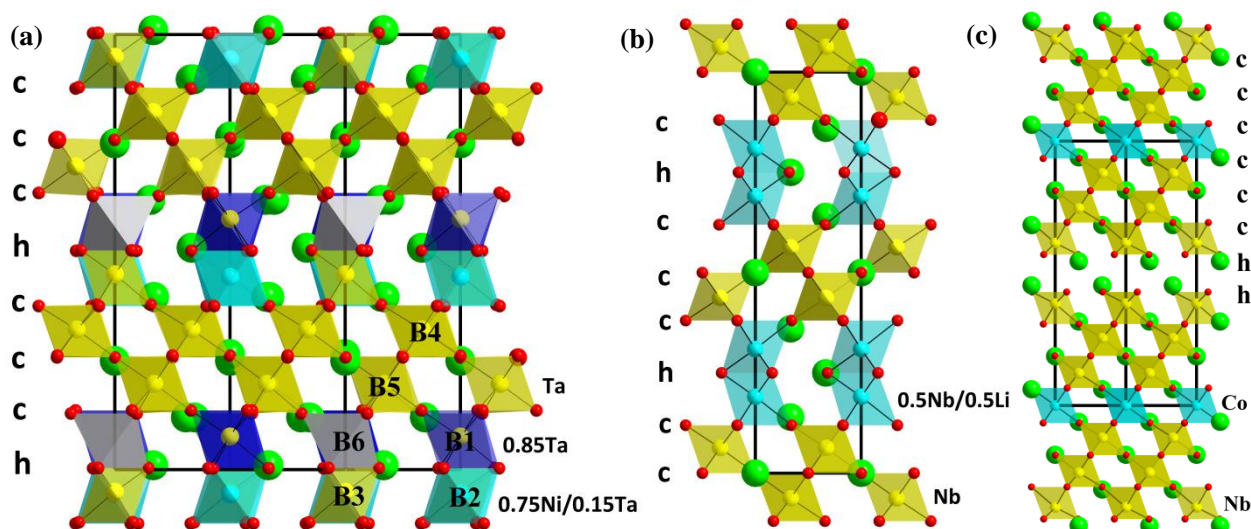


Figure 1. 8-layer hexagonal perovskite structures: twinned $\text{Ba}_8\text{NiTa}_6\text{O}_{24}$ (a) and $\text{Ba}_8\text{Li}_2\text{Nb}_6\text{O}_{24}$ (b), and shifted $\text{Ba}_8\text{CoNb}_6\text{O}_{24}$ (c). In (b) and (c), the octahedral site in yellow is 100% Nb, and cyan is 50% Nb and 50% Li (b) or 100% Co (c). In (a), the octahedral site in yellow is 100% Ta, blue is 85% Ta plus vacancy, and cyan is 75% Ni and 15% Ta plus vacancy; symbols B1-B6 label the six crystallographically distinct B-sites. The empty octahedra are plotted in gray in (a). In (c) the single empty octahedral layers are between the two consecutive hexagonal layers.

Emptying the central octahedral cation layers between two consecutive hexagonal layers in the shifted structure separates the perovskite blocks apart from each other. It is expected that cation ordering similar to those observed in the perovskites may be retained at certain extent in the perovskite blocks of the shifted hexagonal structures. This could offer the chance to produce long-range cation ordering when the perovskite block expands along the stacking direction. The long-range cation ordering is evidenced in the 8-layer shifted $\text{Ba}_8\text{CoNb}_6\text{O}_{24}$ ⁸ by rarely and completely ordered octahedral Co layers 1.88 nm apart in the Nb octahedral host layers: Co cations are located in the central octahedral sites of the perovskite blocks consisting of seven consecutive corner-sharing octahedral (CSO) layers isolated by the single empty octahedral layers (Figure 1c). In this study we report the isolation of $\text{Ba}_8\text{ZnNb}_6\text{O}_{24}$ via controlling the ZnO volatilization and its 8-layer shifted hexagonal perovskite

structure through a carefully structural analysis by a combination of powder X-ray and neutron diffractions, electron diffraction and high resolution transmission electron microscopy. This compound is isostructural with the unusually long-range B-site ordered $\text{Ba}_8\text{CoNb}_6\text{O}_{24}$, featuring nanometer-scale separation of octahedral d^{10} Zn^{2+} layers along the close-packing direction over the solely CSO d^0 Nb^{5+} host layers. The twin-shift preferences of $\text{Ba}_8\text{ZnTa}_6\text{O}_{24}$ and $\text{Ba}_8\text{ZnNb}_6\text{O}_{24}$ emphasize a key role of the subtle difference in oxide-coordination environments between d^0 6-period Ta^{5+} and 5-period Nb^{5+} on the phase stability; it also hints the contribution of the long-range vacancy ordering and out-of-center distortion of the highly-charged d^0 Nb^{5+} cations with more pronounced second-order Jahn-Teller (SOJT) effect to the long-range ordering of Zn^{2+} in the Nb^{5+} host in $\text{Ba}_8\text{ZnNb}_6\text{O}_{24}$. The twin-shift competition of the 8-layer hexagonal perovskite is also demonstrated by the substitutions of d^{10} Sb^{5+} for d^0 Nb^{5+} in

comparison with the Ta⁵⁺ substitution for Nb⁵⁺ in Ba₈ZnNb₆O₂₄. The phase stability is discussed in terms of the multiple factors including the B-cationic sizes, electrostatic repulsion force, long-range ordering of B-site vacancies, bonding preference arising from the covalent contribution to B-O bonding that includes the out-of-center octahedral distortion and B-O-B bonding angle. The ceramics of the new shifted and twinned phases reported here were found to possess good microwave dielectric properties.

Experimental Procedure

The Ba₈ZnNb₆O₂₄, Ba₈ZnNb_{6-x}Sb_xO₂₄ ($x = 0.3, 0.6, 0.9, 1.2, 1.5, 1.8, 2.1, 2.4$) and Ba₈ZnNb_{6-x}Ta_xO₂₄ ($x = 1, 2, 3, 4, 5, 6$) samples were prepared by a routine solid-state reaction, using high purity BaCO₃ (99.99%), ZnO (99.99%), Sb₂O₅ (99.95%), Ta₂O₅ (99.99%) and Nb₂O₅ (99.99%) as starting materials, which were dried at 400 °C for 3 h before weighing. The starting materials were weighed according to the various stoichiometries and mixed in ethanol with an agate mortar, followed by calcinations at 1100 °C for 6 h in alumina crucibles covered with lids with heating and cooling rates of 5 °C/min. In order to investigate how the ZnO volatilization affects the phase formation in Ba₈ZnNb₆O₂₄, preparations under various conditions were carried out. The stoichiometric Ba₈ZnNb₆O₂₄ powders were fired at 1400 °C for 8-24 h, which were compared with the compositions containing 5, 10, 15, 20, 25, 30, 35 and 40 mol% excess ZnO to offset the ZnO volatilization during the high-temperature firing. Also the stoichiometric Ba₈ZnNb₆O₂₄ powders were pressed into pellets and buried in the sacrificial powders of the same compositions in aluminum crucibles covered with lids and fired at 1400 °C for 24 - 36 h with several intermediate grindings and pressings. This method of burying the pellets in the sacrificial powders with the same compositions was found to be effective on obtaining almost pure Ba₈ZnNb₆O₂₄ phase; therefore the synthesis for Ba₈ZnNb_{6-x}Sb_xO₂₄ and Ba₈ZnNb_{6-x}Ta_xO₂₄ samples (including ~ 9 g samples for neutron diffraction and the pellets for electrical characterizations of the Ba₈ZnNb₆O₂₄ and Ba₈ZnNb_{5.1}Sb_{0.9}O₂₄ compositions) were conducted using the same procedure. For the pellets used for the impedance and microwave dielectric property measurements, the pre-calcined powders was mixed with 5% polyvinyl alcohol (PVA) solution as organic binder then pressed into pellets under 330 MPa pressure using a cold isostatic pressing facility, which were heated at 600 °C for 120 min to remove the PVA, followed by firings at 1400 °C for 36 h with heating rate 5 °C/min and cooling rate 0.5 °C/min with two intermediate grindings and pressings. The densities of the pellets were calculated by using the geometric sizes (diameter and thickness) and the masses of the pellets.

The phase assemblages were checked by X-ray powder diffraction (XRD), which was performed on a D8 ADVANCE and Panalytical X'pert Powder X-ray diffractometer with Cu K_α radiation over a 2θ range of 10 - 80° for 20 minutes for each scan. The XRD data with the high quality for Rietveld refinement was collected over a 2θ range of 10 - 120°. Neutron powder diffraction (NPD) data with constant wavelength ($\lambda = 1.6220$ Å) were collected at room temperature on the Echidna high-resolution powder diffractometer at the OPAL facility (Bragg Institute, ANSTO) over a 2θ range of 5 - 160° using a Ge (335)

monochromator. The XRD and NPD data were analyzed by Rietveld refinement²⁷ using Topas Academic software.²⁸ Bond valence sums (BVSs) were calculated by Brown and Altermatt's method.²⁹ The selected area electron diffraction (SAED) and high resolution transmission electron microscopy (HRTEM) images were collected by a JOEL JEM-2100F transmission electron microscope (TEM) with a point resolution of 1.9 Å operated at 200 kV. The surface microstructure of the pellets was examined using a Quanta 400F and Hitachi S4800 scanning electron microscopes (SEM). Prior to the SEM experiment, gold was sprayed on the surface to form a thin conducting layer. The compositions were examined by X-ray energy dispersive spectroscopy (EDS) during the TEM and SEM experiments.

AC impedance spectroscopy measurement was carried out by using a Solartron 1260A impedance/gain-phase analyzer over a temperature range from room temperature to 800 °C and a frequency range from 10⁻¹ Hz to 10⁷ Hz. The pellets were coated with platinum paste and fired at 800 °C for 1 h to remove the organic components to form electrodes. The microwave dielectric properties were measured by the Hakki-Coleman dielectric resonator method³⁰ with the TE₀₁₁ mode using an Agilent N5230A network analyzer. The temperature coefficient of resonant frequency τ_f values were measured from 30 °C to 85 °C.

Results

Isolation of Ba₈ZnNb₆O₂₄. Our preparations show that the phase formation in Ba₈ZnNb₆O₂₄ is highly sensitive to the ZnO volatilization at high temperature. Firing the stoichiometric Ba₈ZnNb₆O₂₄ powder at 1100 °C, 1200 °C and 1300 °C for 24 h at each temperature resulted in mixture of hexagonal perovskite Ba₅Nb₄O₁₅ (5-layer shifted structure, referred to as 5H) and cubic perovskite Ba₃ZnNb₂O₉ (3-layer structure, referred to as 3C) phases (Figure 2a). Increasing the firing temperature to 1400 °C (for 24 h) led to disappearance of the 3C-phase (Figure 2a). This suggests the occurrence of significant ZnO loss during the high-temperature firing at 1400 °C. While shortening the firing time at 1400 °C (to 16 h) led to small amount of the target phase Ba₈ZnNb₆O₂₄ in the products (Figure 2a).

In order to obtain preparation conditions for pure phase Ba₈ZnNb₆O₂₄, the following experimental procedures were conducted for controlling the ZnO loss during the high-temperature firing. The stoichiometric Ba₈ZnNb₆O₂₄ powders were pressed into pellets and fired at 1400 °C in the time range of 4 - 16 h for checking the phase evolution with the firing time. The data indicated that the target phase Ba₈ZnNb₆O₂₄ started to form at 8 h and became a major phase at 12 - 16 h with apparent 5H and 3C impurities in the pressed samples (Figure 2a). This means that the ZnO volatilization was suppressed significantly in the pellets. But this processing did not result in pure phase of Ba₈ZnNb₆O₂₄. To compensate the ZnO volatilization during the firing at high temperature, 5 - 40 mol% excess ZnO were added into the raw powders of Ba₈ZnNb₆O₂₄, which were pressed into pellets and fired at 1400 °C for 4 - 12 h. The XRD data shows that Ba₈ZnNb₆O₂₄ was obtained as the major phase together with the minor 5H and 3C phases under presence of 15 - 40 mol% excess ZnO with a shorter firing time of 8 h (Figure 2b). This indicates that the presence of excess ZnO accelerated the formation of Ba₈ZnNb₆O₂₄. Prolonged firing to 12 h is effective

to remove $\text{Ba}_3\text{ZnNb}_2\text{O}_9$ phase but the longer firing (for 16 h) induced more $\text{Ba}_5\text{Nb}_4\text{O}_{15}$ impurity (Figure 2c), which is ascribed to the increase of ZnO loss with the prolonged firing time. Finally nearly single-phase $\text{Ba}_8\text{ZnNb}_6\text{O}_{24}$ material with tiny amount of 3C phase were obtained via firing the stoichiometric $\text{Ba}_8\text{ZnNb}_6\text{O}_{24}$ pellets buried in the powders with the same composition at 1400 °C for 24 - 36 h with several intermediate grindings and pressings. The XRD pattern of this $\text{Ba}_8\text{ZnNb}_6\text{O}_{24}$ sample is provided in the next section on the structural analysis (Figure 4).

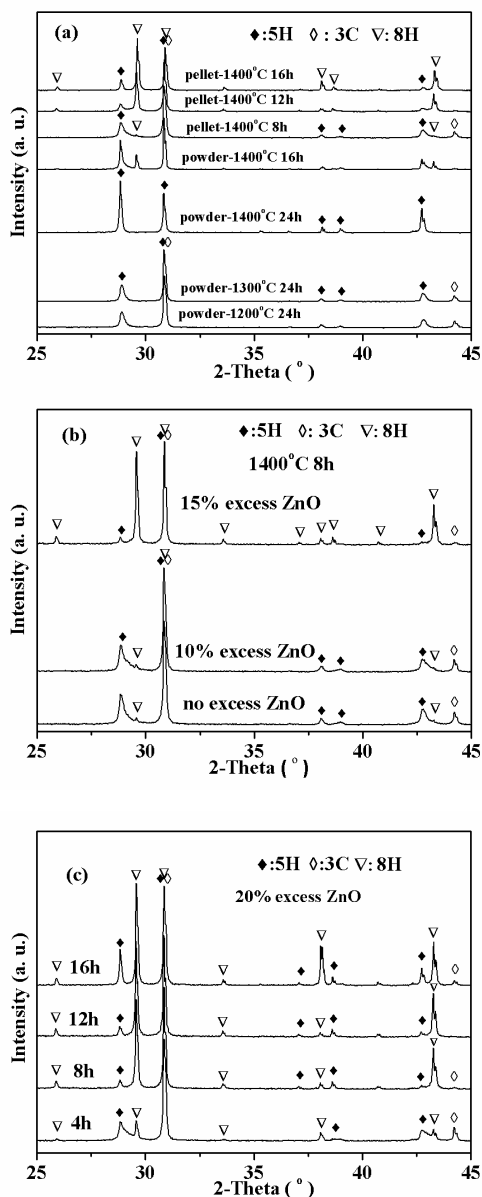


Figure 2. XRD data of various $\text{Ba}_8\text{ZnNb}_6\text{O}_{24}$ samples: (a) stoichiometric $\text{Ba}_8\text{ZnNb}_6\text{O}_{24}$ powder and pellets fired at 1200 - 1400 °C for 8 - 24 h; (b) $\text{Ba}_8\text{ZnNb}_6\text{O}_{24}$ pellets with 0, 10 and 15 mol% excess ZnO fired at 1400 °C for 8 h; (c) $\text{Ba}_8\text{ZnNb}_6\text{O}_{24}$ pellets with 20 mol% excess ZnO fired at 1400 °C for 4 - 16 h.

Shifted structure of $\text{Ba}_8\text{ZnNb}_6\text{O}_{24}$. $\text{Ba}_8\text{ZnNb}_6\text{O}_{24}$ was previously known as an analogue to the twinned $\text{Ba}_8\text{ZnTa}_6\text{O}_{24}$ that adopts an expanded cell by $\sqrt{3}$ in the ab plane of the simple 8-layer hexagonal perovskite cell.¹⁸ However the Rietveld

refinement of $\text{Ba}_8\text{ZnNb}_6\text{O}_{24}$ based on the twinned structure model of $\text{Ba}_8\text{ZnTa}_6\text{O}_{24}$ resulted in a poor fit with Reliability factors $R_{\text{wp}} \sim 10.7\%$, $R_{\text{Bragg}} \sim 11.0\%$ (Figure S1 in supporting information) in this study. Careful examination of the XRD data of $\text{Ba}_8\text{ZnNb}_6\text{O}_{24}$ revealed that its reflections can be also indexed using the simple 8-layer hexagonal perovskite cell ($a \sim 5.793 \text{ \AA}$, $c \sim 18.901 \text{ \AA}$) in space group $P\bar{3}m1$, which is similar to that of the shifted Co-compound $\text{Ba}_8\text{CoNb}_6\text{O}_{24}$.⁸ The electron diffraction patterns (Figure 3a) confirmed this unit cell and symmetry for $\text{Ba}_8\text{ZnNb}_6\text{O}_{24}$. The HRTEM image (Figure 3b) suggested a shifted structure with a stacking sequence of $cchhcc$ for the close-packed BaO_3 layers in $\text{Ba}_8\text{ZnNb}_6\text{O}_{24}$. A combined XRD and NPD Rietveld refinement for $\text{Ba}_8\text{ZnNb}_6\text{O}_{24}$ was performed using the shifted structure model of $\text{Ba}_8\text{CoNb}_6\text{O}_{24}$, which converged to $R_{\text{wp}} \sim 3.82\%$, $R_{\text{Bragg}} \sim 2.06\%$ for XRD data (Figure 4a), and $R_{\text{wp}} \sim 4.82\%$, $R_{\text{Bragg}} \sim 2.77\%$ for NPD data (Figure 4b). This fully confirms that $\text{Ba}_8\text{ZnNb}_6\text{O}_{24}$ adopts the shifted hexagonal perovskite structure instead of the twinned structure in this study. The final refined structural parameters and bond lengths of $\text{Ba}_8\text{ZnNb}_6\text{O}_{24}$ are listed in Tables 1 and 2, respectively.

$\text{Ba}_8\text{ZnNb}_6\text{O}_{24}$ displays complete ordering of Zn^{2+} and Nb^{5+} cations (Table 1): along the c -axis, Zn cations are exclusively located in the central octahedral layers in the seven consecutive CSO layers, which are isolated by the single empty octahedral layers between two consecutive hexagonal BaO_3 layers. Therefore the single octahedral Zn layers are separated by ~ 1.9 nm apart from each other in $\text{Ba}_8\text{ZnNb}_6\text{O}_{24}$, which represents a second rare example of long-range order at nanometer-scale of the solely CSO octahedral cations following the $\text{Ba}_8\text{CoNb}_6\text{O}_{24}$ case. The central octahedral Zn^{2+} site and the outer octahedral Nb^{5+} sites (Nb1-Nb3) in the 7-layer perovskite block have environments (Table 2), respectively, matching well with the centrosymmetric and acentrosymmetric oxide coordination

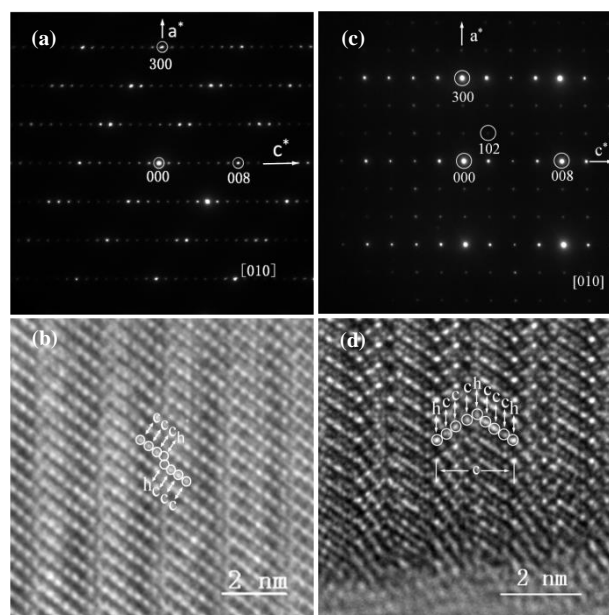


Figure 3. SAED and HRTEM images of the shifted $\text{Ba}_8\text{ZnNb}_6\text{O}_{24}$ (a, b) and the twinned $\text{Ba}_8\text{ZnNb}_{5.1}\text{Sb}_{0.9}\text{O}_{24}$ (c, d): SAED pattern projection along the [010] direction (a) and HRTEM image (b) of the shifted $\text{Ba}_8\text{ZnNb}_6\text{O}_{24}$; SAED pattern projection along the [010] direction (c) and HRTEM image (d) for the twinned $\text{Ba}_8\text{ZnNb}_{5.1}\text{Sb}_{0.9}\text{O}_{24}$.

bonding preference of Zn^{2+} and Nb^{5+} .⁸ The calculated BVSs for Zn and Nb sites (Table 1) agree well with this cation ordering. The centrosymmetric ZnO_6 and typical distorted NbO_6 octahedra are shown in Figure 5a and 5b, respectively.

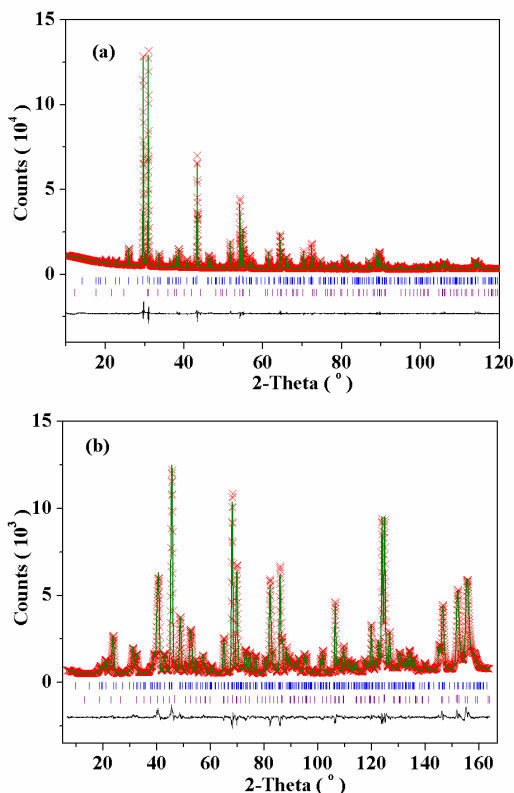


Figure 4. Rietveld refinement plots of XRD (a) and NPD (b) data for the shifted $\text{Ba}_8\text{ZnNb}_6\text{O}_{24}$. The Bragg reflection positions of major phase $\text{Ba}_8\text{ZnNb}_6\text{O}_{24}$ (top) and the minor phase $\text{Ba}_3\text{ZnNb}_2\text{O}_9$ (bottom) are shown by tick marks. The refined weight percentages for $\text{Ba}_8\text{ZnNb}_6\text{O}_{24}$ and $\text{Ba}_3\text{ZnNb}_2\text{O}_9$ are 98.42(7) wt% and 1.58(7) wt%, respectively.

Table 1. The final refined structural parameters for $\text{Ba}_8\text{ZnNb}_6\text{O}_{24}$.*

Atom	Site	x	y	z	Occupancy	$B_{\text{iso}}(\text{\AA}^2)$	BVS
Ba1	2c	0	0	0.1862(1)	1	0.44(1)	2.46
Ba2	2d	1/3	2/3	0.0615(1)	1	0.44(1)	2.25
Ba3	2d	1/3	2/3	0.4544(1)	1	0.44(1)	2.04
Ba4	2d	1/3	2/3	0.6823(1)	1	0.44(1)	2.52
Zn1	1a	0	0	0	1	0.73(8)	1.96
Nb1	2c	0	0	0.3853(1)	1	0.76(9)	4.98
Nb2	2d	1/3	2/3	0.2543(1)	1	0.76(9)	4.65
Nb3	2d	1/3	2/3	0.8781(1)	1	0.76(9)	4.52
O1	6i	0.1681(3)	0.8319(3)	0.3080(1)	1	0.67(1)	2.01
O2	6i	0.1628(2)	0.8372(2)	0.5708(1)	1	0.67(1)	2.15
O3	6i	0.1701(4)	0.8399(4)	0.9339(1)	1	0.67(1)	2.02

* $a = 5.79306(3)$ Å, $c = 18.9035(1)$ Å, $V = 549.399(7)$ Å³, Space group: $P\bar{3}m1$, $Z = 1$.

Shift-to-twin phase transformation. With the aim of obtaining a solid solution of $\text{Ba}_8\text{ZnNb}_{6-x}\text{Sb}_x\text{O}_{24}$ via the Sb^{5+} substitution for Nb^{5+} in $\text{Ba}_8\text{ZnNb}_6\text{O}_{24}$, the $\text{Ba}_8\text{ZnNb}_{6-x}\text{Sb}_x\text{O}_{24}$ samples were synthesized and their XRD patterns are shown in Figure 6a and S2. A quick scan of the XRD data showed that the compositions x

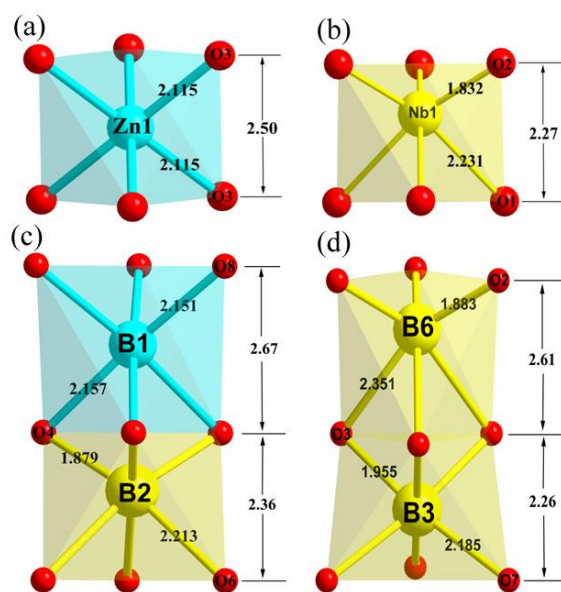


Figure 5. The bonding environments with oxide anions of Zn^{2+} (a) and $(\text{Nb}1)^{5+}$ (b) cations in shifted $\text{Ba}_8\text{ZnNb}_6\text{O}_{24}$ showing the centrosymmetric bonding for Zn^{2+} and asymmetric bonding for Nb^{5+} . (c) and (d) are plots for the FSO dimmers in twinned $\text{Ba}_8\text{ZnNb}_{5.1}\text{Sb}_{0.9}\text{O}_{24}$. The bond lengths (Å) and octahedral thicknesses (Å) are labeled.

Table 2. Bond lengths, octahedral distortion parameters (Δd^*) and B-O-B angles of $\text{Ba}_8\text{ZnNb}_6\text{O}_{24}$.

Bond	Length(Å)	Bond	Length (Å)/Angle (°)
Ba1-O1($\times 3$)	2.854(3)	$\Delta d_{\text{Zn}1}$ (10^{-3})	0
Ba1-O3($\times 3$)	2.841(1)	Nb1-O1($\times 3$)	2.231(3)
Ba1-O4($\times 6$)	2.8967(1)	Nb1-O2($\times 3$)	1.832(1)
Ba2-O3($\times 6$)	2.8981(1)	$\Delta d_{\text{Nb}1}$ (10^{-3})	9.6
Ba2-O3($\times 3$)	2.915(4)	Nb2-O1($\times 3$)	1.944(3)
Ba2-O4($\times 3$)	2.903(4)	Nb2-O4($\times 3$)	2.078(4)
Ba3-O1($\times 3$)	3.227(3)	$\Delta d_{\text{Nb}2}$ (10^{-3})	1.1
Ba3-O2($\times 3$)	2.788(3)	Nb3-O4($\times 3$)	2.099(3)
Ba3-O2($\times 6$)	2.9357(7)	Nb3-O3($\times 3$)	1.948(4)
Ba4-O1($\times 6$)	2.9023(1)	$\Delta d_{\text{Nb}2}$ (10^{-3})	1.4
Ba4-O2($\times 3$)	2.715(3)	Zn1-O3-Nb3	176.57(2)
Ba4-O4($\times 3$)	2.983(3)	Nb1-O1-Nb2	170.57(1)
Zn1-O3($\times 6$)	2.115(4)	Nb2-O4-Nb3	179.03(7)

* $\Delta d = \frac{1}{6} \sum_{n=1-6} \left[\frac{d_n - \langle d \rangle}{\langle d \rangle} \right]^2$, where $\langle d \rangle$ is the average B-O bond length and d_n are the individual B-O bond length.

= 0.3, 0.9, 1.2, 1.5, 1.8, 2.1, 2.4 displayed similar pattern as that of $\text{Ba}_8\text{ZnNb}_6\text{O}_{24}$ except for the minor reflections from the 3C and 5H impurities and unknown phase in $x = 2.4$; on the contrary, the intermediate composition $x = 0.6$ displayed complex XRD pattern with the major reflections split (Figure 6a). The XRD patterns for the compositions $x = 0.3, 0.9, 1.2, 1.5, 1.8, 2.1, 2.4$ were indexed using the cell of shifted $\text{Ba}_8\text{ZnNb}_6\text{O}_{24}$ and the refined cell parameters show a significant gap (Figure S3) between the cell parameters for the compositions $x = 0, 0.3$ and $x = 0.9-2.4$: the a -axis and c -axis jumped to 5.8212(6) Å and 19.0554(3) Å ($x = 0.9$) from 5.7934(4) Å and 18.9049(2) Å ($x = 0.3$), respectively. This abnormal phenomenon coincides with the complex pattern observed on the intermediate composition $x = 0.6$ and indicates that the hexagonal phases in the compositions $x \geq 0.9$ could be

different from the shifted $\text{Ba}_8\text{ZnNb}_6\text{O}_{24}$ phase in the compositions $x \leq 0.3$. Careful examination using Rietveld analysis, ED and HRTEM (which are described in the following section) showed the hexagonal phases in the compositions $x \geq 0.9$ adopt a twinned structure analogue to $\text{Ba}_8\text{ZnTa}_6\text{O}_{24}$ with an expanded cell by $\sqrt{3}$ in the ab plane of the simple 8-layer hexagonal perovskite cell. Therefore the phase formation in $\text{Ba}_8\text{ZnNb}_{6-x}\text{Sb}_x\text{O}_{24}$ can be established as following (Figure S4): the shifted phase retained in the composition $x \leq 0.3$ and it transformed entirely to a twinned phase when $x = 0.9 - 2.1$; while the intermediate composition $\text{Ba}_8\text{ZnNb}_{5.4}\text{Sb}_{0.6}\text{O}_{24}$ (Figure 6a) contained both shifted and twinned phases. The refined cell parameters for the shifted and twinned hexagonal perovskite phases in $\text{Ba}_8\text{ZnNb}_{6-x}\text{Sb}_x\text{O}_{24}$ are given in Figure S4. Increasing the Sb substitution for Nb resulted in mixed phases (Figure 6a) and the end-member $\text{Ba}_8\text{ZnNb}_6\text{O}_{24}$ is a mixture containing $6\text{H}-\text{Ba}_3\text{ZnSb}_2\text{O}_9$ ³¹ and some unknown phases.

Based on the twinned structure for the $\text{Ba}_8\text{ZnTa}_6\text{O}_{24}$ compound, it is expected that Ta substitution for Nb in shifted $\text{Ba}_8\text{ZnNb}_6\text{O}_{24}$ may also induce the shift-to-twin phase transformation at certain composition in $\text{Ba}_8\text{ZnNb}_{6-x}\text{Ta}_x\text{O}_{24}$. Therefore $\text{Ba}_8\text{ZnNb}_{6-x}\text{Ta}_x\text{O}_{24}$ samples were synthesized at 1400 °C for 24 h. Similar to the $\text{Ba}_8\text{ZnNb}_{6-x}\text{Sb}_x\text{O}_{24}$ case, the XRD data (Figure 6b and S5) showed that the shifted structure in $\text{Ba}_8\text{ZnNb}_{6-x}\text{Ta}_x\text{O}_{24}$ transformed to the twinned structure at the $\text{Ba}_8\text{ZnNb}_3\text{Ta}_3\text{O}_{24}$ point, below which $\text{Ba}_8\text{ZnNb}_5\text{TaO}_{24}$ and $\text{Ba}_8\text{ZnNb}_4\text{Ta}_2\text{O}_{24}$ are shifted phase and mixed shifted-twinned phases, respectively. The refined cell parameters for the shifted and twinned hexagonal perovskite phases in $\text{Ba}_8\text{ZnNb}_{6-x}\text{Ta}_x\text{O}_{24}$ are given in Figure S6.

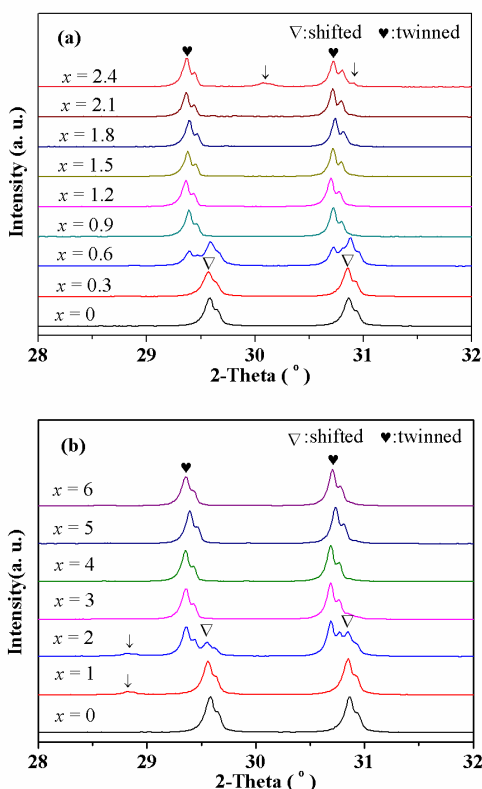


Figure 6. XRD patterns of $\text{Ba}_8\text{ZnNb}_{6-x}\text{Sb}_x\text{O}_{24}$ (a) and $\text{Ba}_8\text{ZnNb}_{6-x}\text{Ta}_x\text{O}_{24}$ (b) in 2-Theta range 28 - 32°, showing the shift-to-twin phase transformation. Symbol ↓ represents reflections from the impurities.

Twined Structure of $\text{Ba}_8\text{ZnNb}_{5.1}\text{Sb}_{0.9}\text{O}_{24}$. The electron diffraction patterns collected on the $\text{Ba}_8\text{ZnNb}_{5.1}\text{Sb}_{0.9}\text{O}_{24}$ composition (Figure 3c) confirmed it adopts the expanded cell ($a \sim 10.1 \text{ \AA}$ and $c \sim 19.1 \text{ \AA}$). The reflection conditions $00l$ ($l = 2n$) and $h0l$ ($l = 2n$) suggest three possible space groups of $P6_3cm$, $P\bar{6}c2$ and $P6_3/mcm$. HRTEM images (Figure 3d) revealed a twinned structure for $\text{Ba}_8\text{ZnNb}_{5.1}\text{Sb}_{0.9}\text{O}_{24}$ with an eight-layer $(ccch)_2$ repeat, analogue to the twinned $\text{Ba}_8\text{ZnTa}_6\text{O}_{24}$. A combined Rietveld refinement of XRD and NPD data of $\text{Ba}_8\text{ZnNb}_{5.1}\text{Sb}_{0.9}\text{O}_{24}$ compound was then performed based on the twinned structure model of $\text{Ba}_8\text{ZnTa}_6\text{O}_{24}$ in $P6_3cm$. In the twinned structure, there are six crystallographically distinct B-sites (Figure 1a): four FSO B-sites B1, B2, B3 and B6 forming two dimers B1-B2 and B3-B6, two CSO B-sites B4 and B5. The site fractional coordinates and the Zn, Nb and Sb occupancies on all the six B-sites in the twinned $\text{Ba}_8\text{ZnNb}_{5.1}\text{Sb}_{0.9}\text{O}_{24}$ were refined without chemical compositional constraint by an approach combining the simulated annealing and Rietveld refinement.^{21, 32} The refinement showed that B3 (FSO), B4 (CSO) and B5 (CSO) sites are fully occupied by Nb(Sb), consistent with their octahedral thicknesses (\AA) 2.26(2) for B3 (Figure 5d), 2.30(1) for B4, 2.28(1) for B5. The other three FSO B1, B2 and B6 are partially occupied, displaying larger octahedral thicknesses (Figure 5c) of 2.67(1), 2.36(1) and 2.61(2), respectively. However, the refined cationic composition $\text{Ba}_8\text{Zn}_{0.05}\text{Nb}_{6.3}\text{Sb}_{0.2}$ contains lower Zn and Sb contents and higher Nb content than those in the nominal composition although the total B-cation content is close to the theoretical value. The bulk cationic composition $\text{Ba}_8\text{Zn}_{0.92(4)}\text{Nb}_{5.3(2)}\text{Sb}_{0.93(1)}$ from the SEM-EDS elementary analysis for $\text{Ba}_8\text{ZnNb}_{5.1}\text{Sb}_{0.9}\text{O}_{24}$ is close to the nominal composition, confirming the existence of Zn and Sb in the twinned sample. Therefore the Zn and Sb atoms in $\text{Ba}_8\text{ZnNb}_{5.1}\text{Sb}_{0.9}\text{O}_{24}$ are not able to be discerned well from the Nb host in the refinement, which is because of their low contents and lower contribution to neutron diffraction (scattering lengths³³ (fm) are 5.57 for Sb, 5.68 for Zn and 7.054 for Nb) i.e. the cationic distribution over the B-sites was not able to be determined unambiguously. Here the bonding environment for each B-site was used to assist the B-cationic and vacancy assignments over the B-sites. The B1 site has symmetric O bonding environment with six $\sim 2.16 \text{ \AA}$ bond lengths, which is perfect for the Zn^{2+} .⁶ All the other B-sites have asymmetric O bonding environments, being suitable for accommodating the Nb^{5+} (Sb^{5+}) cations. Therefore, at next stage, all the Zn^{2+} cations were fixed at B1 sites and occupancies of Nb^{5+} (Sb^{5+}) cations were refined over the other B-sites (B2-B6), which led to a composition of $\text{Ba}_8\text{ZnNb}_{5.5(2)}\text{Sb}_{0.4(2)}$, still showing more Nb and less Sb contents than the expected ones. The refined total occupancies on the B2 and B6 sites are comparable (~ 0.6), which is not consistent with the contrast between their octahedral thicknesses (2.36(1) for B2 and 2.61(2) for B6), implying more cationic occupation on the B2 sites. Therefore the balancing of the overall Nb and Sb contents according to the nominal composition was performed via decreasing the Nb occupancy and increasing Sb occupancy on the B2 sites, which led to the total occupancy 0.71 on the B2 site. The final refinement converged to $R_{wp} \sim 4.51 \%$, $R_{Bragg} \sim 2.31 \%$ on NPD data and $R_{wp} \sim 3.91 \%$, $R_{Bragg} \sim 1.99 \%$ on the XRD data. The Rietveld refinement plots

of XRD and NPD of $\text{Ba}_8\text{ZnNb}_{5.1}\text{Sb}_{0.9}\text{O}_{24}$ are shown in Figure S7. The final refined structural parameters and the interatomic distances of $\text{Ba}_8\text{ZnNb}_{5.1}\text{Sb}_{0.9}\text{O}_{24}$ are listed in Table 3 and S1, respectively. It should be noticed here that local disordered feature (without showing the triple supercell reflections) was observed in the same crystal during the electron diffraction experiments of the $\text{Ba}_8\text{ZnNb}_{5.1}\text{Sb}_{0.9}\text{O}_{24}$ sample. This means that the B-cationic and vacancy ordering in the twinned structure of $\text{Ba}_8\text{ZnNb}_{5.1}\text{Sb}_{0.9}\text{O}_{24}$ sample is not homogenous all through the sample, which could made the average structure from the Rietveld refinement of the powder diffraction data not being able to fully quantitatively describe the cationic and vacancy distribution in the B-sites of $\text{Ba}_8\text{ZnNb}_{5.1}\text{Sb}_{0.9}\text{O}_{24}$.

Table 3. The final refined structural parameters for the twinned $\text{Ba}_8\text{ZnNb}_{5.1}\text{Sb}_{0.9}\text{O}_{24}$.*

Atom	Site	x	y	z	Occupancy	$B_{\text{iso}}(\text{\AA}^2)$	BVS
Ba1	2a	0	0	0.2451(4)	1	0.96(2)	2.27
Ba2	4b	1/3	2/3	0.2403(4)	1	0.96(2)	2.52
Ba3	6c	0.6630(8)	0	0.6066(1)	1	0.96(2)	2.48
Ba4	6c	0.3218(5)	0	0.8778(1)	1	0.96(2)	2.02
Ba5	6c	0.3339(9)	0	0.4901(3)	1	0.96(2)	2.06
Zn1	4b	1/3	2/3	0.4274(6)	0.75	0.52(2)	1.78
Nb2	4b	1/3	2/3	0.0499(6)	0.22	0.52(2)	4.60
Sb2	4b	1/3	2/3	0.0499(6)	0.49	0.52(2)	5.01
Nb3	2a	0	0	0.0568(5)	1	0.52(2)	4.10
Nb4	6c	0.3382(9)	0	0.6774(3)	1	0.52(2)	4.80
Nb5	6c	0.6663(8)	0	0.8022(3)	0.91(4)	0.52(2)	4.53
Sb5	6c	0.6663(8)	0	0.8022(3)	0.09(5)	0.52(2)	4.93
Nb6	2a	0	0	0.9032(7)	0.48(9)	0.52(2)	4.14
Sb6	2a	0	0	0.9032(7)	0.10(7)	0.52(2)	4.51
O1	6c	0.4976(5)	0	0.2416(6)	1	0.89(2)	2.02
O2	6c	0.1665(7)	0.1665(7)	0.8584(6)	1	0.89(2)	2.32
O3	6c	0.1552(3)	0.1552(3)	0.4953(3)	1	0.89(2)	1.92
O4	12d	0.6643(1)	0.1701(1)	0.5013(3)	1	0.89(2)	1.79
O5	12d	0.3337(7)	0.1663(7)	0.2388(4)	1	0.89(2)	1.92
O6	12d	0.6621(3)	0.1641(1)	0.1253(3)	1	0.89(2)	1.98
O7	6c	0.1881(9)	0.1881(9)	0.1137(5)	1	0.89(2)	2.10
O8	12d	0.4868(9)	0.3184(9)	0.8613(4)	1	0.89(2)	1.77

* $a = 10.08267(2)$ \AA, $c = 19.05159(6)$ \AA, $V = 1677.31(1)$ \AA³, Space group: $P6_3cm$, $Z = 3$. Zn1, Nb2/Sb2, Nb3, Nb4 Nb5/Sb5, Nb6/Sb6 sites correspond to B1, B2, B3, B4, B5 and B6 sites in Figure 1a, respectively.

Electrical properties and Microstructure. The as-made $\text{Ba}_8\text{ZnNb}_6\text{O}_{24}$ pellet (~ 92 % of theoretical density) displayed $\epsilon_r \sim 35$, $Qf \sim 24883$ GHz. After being annealed at 1000 °C for 48 h, the $\text{Ba}_8\text{ZnNb}_6\text{O}_{24}$ ceramic displayed a better quality factor $Qf \sim 43400$ GHz and its temperature coefficient of resonate frequency τ_f is ~ 38 ppm/°C. The as-made twinned $\text{Ba}_8\text{ZnNb}_{5.1}\text{Sb}_{0.9}\text{O}_{24}$ pellet (~ 95 % of theoretical density) displayed the same $\epsilon_r \sim 35$ as that for $\text{Ba}_8\text{ZnNb}_6\text{O}_{24}$ but lower $Qf \sim 36200$ GHz and higher $\tau_f \sim 44$ ppm/°C compared with the annealed $\text{Ba}_8\text{ZnNb}_6\text{O}_{24}$. On the contrary, annealing at 1000 °C (for 48 h) deteriorated the Qf value to 26900 GHz for $\text{Ba}_8\text{ZnNb}_{5.1}\text{Sb}_{0.9}\text{O}_{24}$ pellet.

Impedance data of the $\text{Ba}_8\text{ZnNb}_6\text{O}_{24}$ and $\text{Ba}_8\text{ZnNb}_{5.1}\text{Sb}_{0.9}\text{O}_{24}$ pellets consist of a large semicircular and a small semicircular arcs (Figure S8) corresponding to the bulk and grain boundary responses, respectively. No electrode response was observed in the $\text{Ba}_8\text{ZnNb}_6\text{O}_{24}$ and $\text{Ba}_8\text{ZnNb}_{5.1}\text{Sb}_{0.9}\text{O}_{24}$ pellets. The typical complex impedance plot for $\text{Ba}_8\text{ZnNb}_6\text{O}_{24}$ at 800 °C is shown in Figure S8a. The bulk resistivity of $\text{Ba}_8\text{ZnNb}_6\text{O}_{24}$ pellet was estimated as the intercept of the large semicircular arc at low

frequency and the associated C estimated from the equation $\omega RC = 1$ ($\omega = 2\pi f_{\text{max}}$, ω is angular frequency, f_{max} is the frequency corresponding to the maximum Z'') is ~ 3.3 pF/cm, consistent with the bulk response³⁴ and the permittivity measured at microwave frequency. The bulk conductivity of the $\text{Ba}_8\text{ZnNb}_6\text{O}_{24}$ ceramic varied within 10^{-9} - 10^{-6} S/cm in 400 - 800 °C (Figure S9) and the activation energies (E_a) showing an increase from 0.77(2) eV in low temperature region below 600 °C to 1.49(6) eV above 600°C. The twinned $\text{Ba}_8\text{ZnNb}_{5.1}\text{Sb}_{0.9}\text{O}_{24}$ pellet displayed higher bulk conductivities (Figure S9) ~ 10^{-8} - 10^{-5} S/cm within 500 - 800 °C than those for $\text{Ba}_8\text{ZnNb}_6\text{O}_{24}$. Similar curvature of the Arrhenius plot of bulk conductivity occurred on the $\text{Ba}_8\text{ZnNb}_{5.1}\text{Sb}_{0.9}\text{O}_{24}$ pellet, leading to higher activation energy (1.58(5) eV) above 600 °C than that (1.04(3) eV) below 600 °C (Figure S9). Such a phenomenon on the activation energies may be ascribed to change of conduction mechanism to the electronic conduction in high temperature over the intrinsic band gap from the impurity ionization in low temperature region, which is similar to the cases of $\text{Ba}_8\text{Ga}_{4-x}\text{Ta}_{4+0.6x}\text{O}_{24}$ ²¹ and $\text{Ba}_8\text{ZnTa}_6\text{O}_{24}$ ¹⁸ pellets.

The surface morphologies of $\text{Ba}_8\text{ZnNb}_6\text{O}_{24}$ and $\text{Ba}_8\text{ZnNb}_{5.1}\text{Sb}_{0.9}\text{O}_{24}$ pellets were examined by SEM, which are shown in Figure S10. The surface of $\text{Ba}_8\text{ZnNb}_6\text{O}_{24}$ pellet (Figure S10a) displays mainly bar-shaped grains with ~ 50 - 100 μm lengths and ~ 10 - 30 μm widths. Similar grain growth has been widely observed other 8-layer hexagonal perovskites including $\text{Ba}_8\text{ZnTa}_6\text{O}_{24}$,¹⁷ $\text{Ba}_8\text{NiTa}_6\text{O}_{24}$,³⁵ $\text{Ba}_8\text{Ti}_3\text{Nb}_4\text{O}_{24}$,³⁶ $\text{Ba}_8\text{CuTa}_6\text{O}_{24}$ ³⁷ and $\text{Ba}_8\text{Ga}_{4-x}\text{Ta}_{4+0.6x}\text{O}_{24}$.²¹ The surface of the $\text{Ba}_8\text{ZnNb}_{5.1}\text{Sb}_{0.9}\text{O}_{24}$ pellet (Figure S10b) is different with that in $\text{Ba}_8\text{ZnNb}_6\text{O}_{24}$ pellet: apart from the column-shaped grains with smaller widths and lengths, the plate-shaped grains were often observed.

Discussion

The twin-shift competition of the 8-layer hexagonal perovskites observed in $\text{Ba}_8\text{ZnNb}_{6-x}\text{Sb}_x\text{O}_{24}$ and $\text{Ba}_8\text{ZnNb}_{6-x}\text{Ta}_x\text{O}_{24}$ here is summarized in Table S2 together with the previous reported B-site deficient 8-layer twinned and shifted $\text{Ba}_8\text{B}_7\text{O}_{24}$ compounds as well for comparison. Among these 8-layer hexagonal perovskites, the twinned-structure preference for the tantalates/Ta-rich compositions is still reserved. The twin-shift phase competition has been discussed by Troliard *et al* within a more wide composition range of $A_n\text{B}_{n-1}\text{O}_{3n}$ ($n = 4 - 8$),³⁸ which formed exclusively shifted phase for the small n values (4 - 7) except for the $n = 8$ composition displaying the twin-shift competition. The twinned structure of $A_8\text{B}_7\text{O}_{24}$ contains 50 % B-□ (□ denotes B-site vacancy) and 50 % B-B in the FSO dimers; while for the shifted structure, the emptying of central octahedral sites in the FSO trimers removes the short FSO B-B contacts thus effectively minimizes the electrostatic repulsion force among the B-cations. Troliard *et al* argued that $A_n\text{B}_{n-1}\text{O}_{3n}$ forms the shifted structure to avoid the strong FSO B-B repulsion at cost of the energy for establishing the long-range ordering of B-site vacancies, which become more difficult when the n value increases (no shifted phase formed for $n = 9$ with a longer periodicity than that in $n = 8$ shifted member); on the contrary, forming the twinned structure is useful for decreasing drastically the periodicity of B-site vacancies, which is coupled by the partial ordering within *ab*-plane of the cations and vacancies

among the FSO sites to reduce the FSO B-B repulsive interactions.³⁸ No $n = 10$ twinned members of $A_nB_{n-1}O_{3n}$ was found although the 10-layer twinned structure formed on $A_nB_{n-2}O_{3n}$ -type $Ba_{10}Mg_{0.25}Ta_{7.9}O_{30}$ and $Ba_{10}Ti_{1.2}Ti_{7.04}O_{30}$ compositions because of they are free of FSO B-B pairs.^{19, 38} Therefore, in the compounds with large n value (8), the balance between the long-range ordering of B-site vacancies and FSO B-B repulsive force but with short periodicity of B-site vacancies results in the twin-shift phase competition. The electrostatic force and B-cationic size may be considered as two important factors to interpret the twin-to-shift transformation upon the substitution of $(Lu^{3+}_{0.5}Nb^{5+}_{0.5})$ for Ti^{4+} in $Ba_8Ti_{3-2x}Nb_{4+x}Lu_xO_{24}$ system.³⁸ The substitution of the mixed cations $Lu^{3+}_{0.5}Nb^{5+}_{0.5}$ for the smaller Ti^{4+} cations in the twinned structure could induce severe electrostatic repulsion in the FSO dimer, thus destabilizing the twinned phase and driving the transformation to shifted structure with reduced B-cationic electrostatic repulsion.

In case of $Ba_8ZnNb_{6-x}M_xO_{24}$ ($M = Sb, Ta$) here, the isoivalent substitutions across the shift-to-twin transformations do not change the B-cationic size very much: the average B-cationic size is reduced by 0.005 Å in the Sb-substituted material $Ba_8ZnNb_{5.1}M_{0.9}O_{24}$ and remains unchanged in the Ta-substituted materials (Table S2), in great contrast with the change of average B-cationic size (0.021 Å) in $Ba_8Ti_{3-2x}Nb_{4+x}Lu_xO_{24}$ (Table S2). This might indicate that the cationic size effect and electrostatic repulsion force are minor factors for the twin-shift competition in $Ba_8ZnNb_{6-x}M_xO_{24}$ ($M = Sb, Ta$) cases. Here the bonding preference from the covalency of B-O bonds is taken in account for understanding the twin-shift phase competition in the $Ba_8ZnNb_{6-x}M_xO_{24}$ as well as the twinned-structure preference for the $Ba_8B_7O_{24}$ tantalates, in addition to the factors that include the electrostatic force, the long-range or short-range vacancy ordering and the B-cationic size. The covalent contribution to the B-O bonds, which represents the electronic energy and affects the bonding preference of B-cations, has been regarded as the major one of four principal factors affecting the phase stability of $A^+B^{5+}O_3$ containing Nb^{5+} , Ta^{5+} and Sb^{5+} that includes relative

ionic size, electrostatic force (representing the Madelung or lattice energy), polarizability of A-cation cores as well.^{39, 40} As our discussion is focusing on the $Ba_8B_7O_{24}$ compositions, the size and polarizability of A-cations are not considered as the primary factors affecting the twin-shift stability of $Ba_8B_7O_{24}$ described here.

It is well known that the d^0 cations of the 6-period Ta^{5+} and 5-period Nb^{5+} have the same ionic sizes owing to the lanthanide contraction and close electronegativity; as a result, they have close chemical bonding preferences, which make that many niobates have isostructural Ta-analogues.⁶ The strong preference of the twinned structure over the shifted structure for the tantalates compared with the niobates in the 8-layer hexagonal perovskites may result from different covalency on the bonding with oxide anions (*i.e.* oxide-coordination environment) of Ta^{5+} and Nb^{5+} cations, which could be subtle but induce significant impact on the twin-shift phase stabilization in 8-layer hexagonal perovskites. Electronic calculations and experimental measurements in a wide range of cubic perovskite and its layered derivatives have indicated that the Nb^{5+} is more covalent than Ta^{5+} .⁴¹ The empty d orbitals result in SOJT distortions in octahedra containing Ta^{5+} and Nb^{5+} , showing multiple bond lengths with oxygen and out-of-center displacement in the octahedra.^{42, 43} The more covalent Nb^{5+} has increased preference and energy stability gain for the out-of-center displacement compared with Ta^{5+} , which is consistent that the occurrence of more symmetric coordination environment of Ta^{5+} compared with Nb^{5+} observed in many 2:1-ordered complex perovskites⁶ and simple perovskites⁴⁴⁻⁴⁶ of tantalates and niobates. This subtle difference in the oxide ion coordination environment between Nb^{5+} and Ta^{5+} has been shown as driving force of the ordering/segregation between Nb^{5+} and Ta^{5+} into layers in a 1:1 ratio in $NaNb_{1-x}Ta_xO_3$.¹¹ The stronger covalency of the Nb^{5+} -O bonds than the Ta^{5+} -O bonds is also evidenced by the fact that the dielectric permittivities of the Ta^{5+} -containing materials are lower than the Nb^{5+} -containing analogues.^{6, 8, 21}

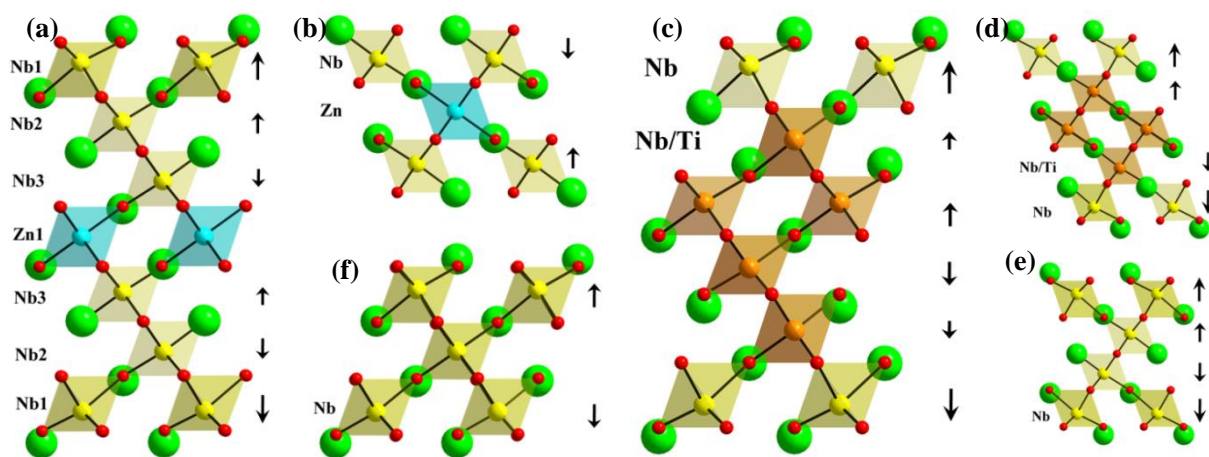


Figure 7. Perovskite blocks of some typical Nb^{5+} -containing shifted $A_nB_{n-1}O_{3n}$ hexagonal perovskites showing the common feature of the out-of-center octahedral distortion: (a) $Ba_8ZnNb_6O_{24}$ ($n = 8$) (in comparison with the (b) $Ba_3ZnNb_2O_9$ complex perovskite), (c) $Ba_7Nb_4Ti_2O_{21}$ ($n = 7$), (d) $Ba_6NbTi_4O_{18}$ ($n = 6$), (e) $Ba_5Nb_4O_{15}$ ($n = 5$), and (f) $Ba_3LaNb_3O_{12}$ ($n = 4$). The arrows denote the displacement directions of octahedral B-cations and their lengths roughly mark the relative displacement tensors in each plot.

In the 8-layer ordered shifted structure, all the NbO_6 octahedra display out-of-center distortion, where the Nb^{5+} centers are

displaced along different directions and at different tenses (Figure 7a). This structural feature of the cooperative octahedral

distortion is common in the B-site deficient $A_nB_{n-1}O_{3n}$ shifted structures⁴⁷⁻⁵⁰ (Figure 7), which could appear as an important factor for stability of shifted phase. The octahedral distortion generally comes from the electronic and structural components in the bond network. The SOJT effect of the highly-charged d^0 cations (e.g. W^{6+} , Nb^{5+} , Ta^{5+} , Ti^{4+}) in the materials assists the out-of-center distortion, which is required for satisfying the coordination environments of the oxide anions.⁶ The distortion extends for the inner Nb_2O_6 and Nb_3O_6 octahedra (Figure 7a and Table 2) in the perovskite block of $Ba_8ZnNb_6O_{24}$ and $Ba_8CoNb_6O_{24}$ are close to those observed in complex perovskites (Figure 7b),^{6, 8} while the Nb_1O_6 octahedral layers in edge of the perovskite block next to the empty octahedra demonstrate the much severer distortion (Table 2) with displacement of Nb^{5+} toward tri-oxygen face in the empty octahedral, forming three short bonds with the oxygen atoms in the empty octahedra (Figure 5b and Table 2). Such strong distortion of the edge octahedra containing highly-charged cation centers is essential for stabilizing the oxide anions of the empty octahedra in the shifted structure. Therefore the long-range ordering B-site vacancy and the SOJT distortion of highly-charged d^0 Nb^{5+} cations are considered as major driving forces for the long-range ordering of d^{10} Zn^{2+} layer in the central positions of the perovskite blocks in $Ba_8ZnNb_6O_{24}$, which is also assisted by the size difference between Zn^{2+} and Nb^{5+} . This mechanism may be also applicable to $Ba_8CoNb_6O_{24}$ compound.⁸ Replacing Nb^{5+} using the more ionic Ta^{5+} showing more symmetric coordination environment would not be ideal for stabilizing the oxide anions in the empty octahedral layers. Although the Nb^{5+} cations in the five layer shifted $Ba_5Nb_4O_{15}$ can be replaced fully by Ta^{5+} to form a stable Ta-analogue, the non-accessibility of the shifted $Ba_8ZnTa_6O_{24}$ may be ascribed to that the long-range ordering of vacancy over a longer distance ~ 19 Å (versus ~ 12 Å in the 5-layer structure) in the non-ideal Ta^{5+} host would cost more energy, which is not practical for stabilizing the shift structure. This drives phase transformation upon the Ta^{5+} substitution for Nb^{5+} in $Ba_8ZnNb_6O_{24}$ to the twinned structure with shorter periodicity of B-site vacancies. The B-site vacancy ordering in the twinned structure of $Ba_8ZnTa_6O_{24}$ may optimize the electrostatic repulsion force in the FSO dimers via forming Ta^{5+} -□ and Zn^{2+} - Ta^{5+} pairs.^{18, 19, 38} The latter pair is rare but has been observed in $Zn_3Ta_2O_8$.⁵¹

In the Sb-substituted $Ba_8ZnNb_6O_{24}$, the difference in the bonding preference between the d^0 Nb^{5+} and d^{10} Sb^{5+} cations associated with the covalency of B-O bonding may also play a key role in stabilization of the twinned structure. In the B-site-vacancy-ordered structure of shifted $Ba_8ZnNb_6O_{24}$, the CSO perovskite blocks are isolated by the single empty octahedral layers among the two hexagonal BaO_3 layers; therefore all of the B-O-B linkages are close to 180° (Table 2), which match well with the d^0 Nb^{5+} cations with empty d shells that participate strongly in the π -bonding in the linear B-O-B bonds (Figure 8a). While the filled d^{10} orbitals in Sb^{5+} cation do not participate in the π -bonding thus favors the 90° B-O-B bonds (Figure 8b) over the linear B-O-B bonds; the 90° geometry of B-O-B bonds optimizes the σ -bonding of Sb^{5+} with two different O 2p orbitals for each B-O bond (Figure 8b), which leads to stronger covalent contribution to B-O bonds in the Sb^{5+} -containing compositions.³⁹

40 When the Sb-substitution amount in $Ba_8ZnNb_{6-x}Sb_xO_{24}$ is small ($x \leq 0.3$), the Sb^{5+} is diluted in the Nb^{5+} host for preventing from formation of linear Sb-O-Sb bonds thus forming a shift-type solid solution. The increase of Sb^{5+} substitution enhances probability of Sb^{5+} centers sitting in two corner-shared octahedra that leads to near-linear Sb-O-Sb bonds in the perovskite blocks, which may destabilize the shifted structure. In the twinned structure, the 90° B-O-B bonds in the FSO dimers (either Zn^{2+} -O- B^{5+} or B^{5+} -O- B^{5+}) meet the Sb^{5+} bonding preference, thus driving the shift-to-twin transformation in $Ba_8ZnNb_{6-x}Sb_xO_{24}$ upon the Sb^{5+} substitution for Nb^{5+} . Similar structure transformation upon the Sb^{5+} substitution for Nb^{5+} has been observed in $Ba_3MnNb_{2-x}Sb_xO_9$ ($M = Mg, Ni, Zn$): the structure transformed from the 2:1-ordered complex perovskite ($Ba_3MnNb_2O_9$) to the 6H-BaTiO₃-type hexagonal perovskite ($Ba_3MSb_2O_9$)³¹ containing FSO dimer Sb_2O_9 units. In $Ba_8ZnNb_{6-x}Sb_xO_{24}$, it is the distinct bonding preferences of d^0 Nb^{5+} and d^{10} Sb^{5+} that make the small Sb^{5+} -substitution ($\sim 15\%$) being significant to drive shift-to-twin phase transformation. While the subtle contrast in the covalency/oxide-anion coordination environment between Ta^{5+} and Nb^{5+} makes the shift-to-twin transformation to occur at the highly Ta^{5+} -substituted composition ($\sim 50\%$) in $Ba_8ZnNb_{6-x}Ta_xO_{24}$.

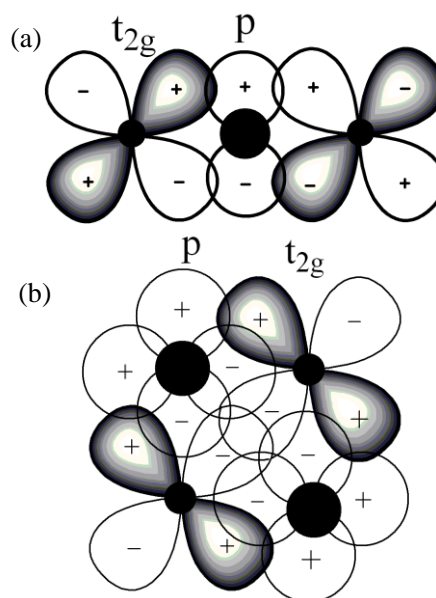


Figure 8. Schematic plots for π -bonding in 180° (a) and σ -bonding in 90° (b) B-O-B bonds involving transition-metal-cation t_{2g} and O 2p orbitals, according to Goodenough et al.³⁹ In (b), the σ -bonding involves two different O 2p orbitals used for each B-O bond.

In the twinned $Ba_8ZnNb_{6-x}Sb_xO_{24}$, Sb^{5+} cations are expected to preferably occupy the FSO sites although the structure refinement is not able to discern well the Sb^{5+} in the Nb^{5+} host. The partial ordering of cations and vacancies among the FSO B-sites (B1-B2 and B3-B6 dimers) may optimize the electrostatic repulsion between FSO cation via locally placing the B^{5+} -□ pair at high priority in FSO site in the way that works in $Ba_8MTa_6O_{24}$ ($M = Zn$ and Ni) cases.^{18, 19, 55} As revealed by the refinement and ED study, the distribution of B-cation and B-site vacancies in the twinned $Ba_8ZnNb_{5.1}Sb_{0.9}O_{24}$ is more disordered than that in $Ba_8MTa_6O_{24}$ ($M = Zn, Ni$)^{18, 19, 55} and $Ba_8Ga_{0.8}Ta_{5.2}O_{24}$.²¹ This implies that in $Ba_8ZnNb_{5.1}Sb_{0.9}O_{24}$ the FSO Nb^{5+} - Nb^{5+} pairs have

large probability in addition to FSO Sb^{5+} - Sb^{5+} , as indicated by the large occupancy of $0.40\text{Nb}^{5+}/0.10\text{Sb}^{5+}$ on B6 site and fully occupied B3 sites solely by Nb^{5+} for the FSO B3-B6 dimers from the refinement results of $\text{Ba}_8\text{ZnNb}_{5.1}\text{Sb}_{0.9}\text{O}_{24}$ (Table 3), which is in contrast with $\text{Ba}_8\text{MTa}_6\text{O}_{24}$ showing that the B6 sites are completely empty among the four FSO B-sites.^{18, 19, 38, 55} Although it is rare, the occurrence of FSO Nb^{5+} - Nb^{5+} dimers has been observed in $\text{Ba}_4\text{Nb}_2\text{O}_9$ and $\text{Mg}_4\text{Nb}_2\text{O}_9$ compounds.⁵⁶⁻⁵⁸ The FSO dimers containing highly-charged Nb^{5+} (Ta^{5+}) are expected to be unstable because of the strong electrostatic repulsion force in the FSO dimers. However, according to Blasse,⁵⁹ the spatial distribution of the B^{5+} - O^{2-} - B^{5+} π -bonding electrons along the B-B axis may provide some B-B bonding, which stabilizes the FSO dimers containing Nb^{5+} and Ta^{5+} .

Conclusions

8-layer shifted hexagonal perovskite $\text{Ba}_8\text{ZnNb}_6\text{O}_{24}$ was isolated through controlling the ZnO volatilization at high temperature, which features complete ordering of the Nb^{5+} and Zn^{2+} cations, forming unusual nanometer-scale separation of octahedral d^{10} Zn^{2+} layer in the purely CSO d^0 Nb^{5+} host. Small amount (~15 %) of Sb^{5+} substitution for Nb^{5+} in $\text{Ba}_8\text{ZnNb}_6\text{O}_{24}$ transformed the crystal structure to a twinned structure analogue to $\text{Ba}_8\text{ZnTa}_6\text{O}_{24}$, in contrast with the $\text{Ba}_8\text{ZnNb}_{6-x}\text{Ta}_x\text{O}_{24}$ case requiring 50 % Ta substitution for Nb for the shift-to-twin phase transformation. The ceramics of new shifted $\text{Ba}_8\text{ZnNb}_6\text{O}_{24}$ and twinned $\text{Ba}_8\text{ZnNb}_{5.1}\text{Sb}_{0.9}\text{O}_{24}$ compounds exhibited good microwave dielectric properties: ($\epsilon_r \sim 35$, $Q_f \sim 36200 - 43400$ GHz and $\tau_f \sim 38 - 44$ ppm/°C). Multiple factors including B-cationic sizes, electrostatic repulsion force, long-range ordering of B-cationic vacancies, and bonding preferences from the covalent contribution to B-O bonding that includes out-of-center octahedral distortion and B-O-B bonding angle could subtly contribute to the twin-shift phase competition in B-site deficient 8-layer hexagonal perovskites $\text{Ba}_8\text{B}_7\text{O}_{24}$. This study elucidates a key role of long-range ordering of B-cationic vacancies and out-of-center octahedral distortion of highly-charged Nb^{5+} with more pronounced SOJT effect on the nanometer-scale long-range ordering of d^{10} Zn^{2+} layer in d^0 Nb^{5+} host in the shifted structure. The roles of differences in the bonding preferences among d^{10} Sb^{5+} , d^0 Nb^{5+} and d^0 Ta^{5+} cations with oxide anions on controlling the phase stability are emphasized by the shift-to-twin phase transformation in the 8-layer hexagonal perovskites $\text{Ba}_8\text{ZnNb}_{6-x}\text{M}_x\text{O}_{24}$ (M = Sb, Ta).

Acknowledgments

The National Natural Science Foundation of China (No. 21361008), Guangdong Natural Science Foundation (S2011010001310), Guangxi Program for Hundred Talents for Returned Scholars and Guangxi Key Laboratory for Advanced Materials and New Preparation Technology (No. 12AA-11) are acknowledged for the financial support. We gratefully acknowledge the support from Bragg Institute in Australian Nuclear Science and Technology Organisation (ANSTO) and the assistance of Dr. James Hester on the NPD experiments using the high-resolution powder diffractometer Echidna (Proposal No. P3525).

Notes and references

- ^a Guangxi Ministry-Province Jointly-Constructed Cultivation Base for State Key Laboratory of Processing for Nonferrous Metal and Featured Materials, Guangxi Universities Key Laboratory of Non-ferrous Metal Oxide Electronic Functional Materials and Devices, College of Materials Science and Engineering, Guilin University of Technology, Guilin 541004 P. R. China. Fax: +86-773-5896 070; Tel: 86-773-5896 070; E-mail: kuangxj@gult.edu.cn.
- ^b Beijing National Laboratory for Molecular Sciences, The State Key Laboratory of Rare Earth Materials Chemistry and Applications, College of Chemistry and Molecular Engineering, Peking University, Beijing 100871, P. R. China. Fax: +86 010-6275 4188; Tel: +86 010-6275 4188; E-mail: xijing@pku.edu.cn.
- ^c MOE Key Laboratory of Bioinorganic and Synthetic Chemistry, State Key Laboratory of Optoelectronic Materials and Technologies, School of Chemistry and Chemical Engineering, Sun Yat-Sen University, Guangzhou 510275, P. R. China.
- ^d Instrumental Analysis and Research Center, Sun Yat-Sen University, Guangzhou 510275, P. R. China.
- [†] Electronic Supplementary Information (ESI) available: Rietveld refinement plot of XRD data for $\text{Ba}_8\text{ZnNb}_6\text{O}_{24}$ based on the twinned structure; refined cell parameters of $\text{Ba}_8\text{ZnNb}_{6-x}\text{Sb}_x\text{O}_{24}$ based on the shifted $\text{Ba}_8\text{ZnNb}_6\text{O}_{24}$ structure; Rietveld refinement plots of XRD and NPD data and interatomic distances for twinned $\text{Ba}_8\text{ZnNb}_{5.1}\text{Sb}_{0.9}\text{O}_{24}$; XRD patterns of $\text{Ba}_8\text{ZnNb}_{6-x}\text{Sb}_x\text{O}_{24}$ and $\text{Ba}_8\text{ZnNb}_{6-x}\text{Ta}_x\text{O}_{24}$; refined cell parameters of the twinned and shifted phases in $\text{Ba}_8\text{ZnNb}_{6-x}\text{Sb}_x\text{O}_{24}$ and $\text{Ba}_8\text{ZnNb}_{6-x}\text{Ta}_x\text{O}_{24}$; complex impedance plots at 800 °C, Arrhenius plots of bulk conductivity and SEM images of $\text{Ba}_8\text{ZnNb}_6\text{O}_{24}$ and $\text{Ba}_8\text{ZnNb}_{5.1}\text{Sb}_{0.9}\text{O}_{24}$ pellets; twin-shift option, average B-cationic sizes, and the tolerance factors of the B-site deficient 8-layer hexagonal perovskites $\text{Ba}_8\text{B}_7\text{O}_{24}$; crystallographic information files in CIF format of shifted $\text{Ba}_8\text{ZnNb}_6\text{O}_{24}$ and twinned $\text{Ba}_8\text{ZnNb}_{5.1}\text{Sb}_{0.9}\text{O}_{24}$. See DOI: 10.1039/b000000x/
- Davies, P. K., *Curr. Opin. Solid State Mat. Sci.* **1999**, 4, 467-471.
- Huang, Y. H.; Karppinen, M.; Yamauchi, H.; Goodenough, J. B., *Phys. Rev. B* **2006**, 73, 104408.
- Reaney, I. M.; Iddles, D., *J. Am. Ceram. Soc.* **2006**, 89, 2063-2072.
- Davies, P. K.; Wu, H.; Borisevich, A. Y.; Molodetsky, I. E.; Farber, L., *Ann. Rev. Mater. Res.* **2008**, 38, 369-401.
- Harada, Y.; Hirakoso, Y.; Kawai, H.; Kuwano, J., *Solid State Ionics* **1999**, 121, 245-251.
- Lufaso, M. W., *Chem. Mater.* **2004**, 16, 2148-2156.
- Kuang, X.; Claridge, J. B.; Price, T.; Iddles, D. M.; Rosseinsky, M. J., *Inorg. Chem.* **2008**, 47, 8444-8450.
- Mallinson, P. M.; Allix, M. M. B.; Claridge, J. B.; Ibberson, R. M.; Iddles, D. M.; Price, T.; Rosseinsky, M. J., *Angew. Chem. Int. Ed.* **2005**, 44, 7733-7736.
- Guiton, B. S.; Davies, P. K., *Nat. Mater.* **2007**, 6, 586-591.
- García-Martín, S.; Urones-Garrote, E.; Knapp, M. C.; King, G.; Woodward, P. M., *J. Am. Chem. Soc.* **2008**, 130, 15028-15037.
- Torres-Pardo, A.; Krumeich, F.; González-Calbet, J. M.; García-González, E., *J. Am. Chem. Soc.* **2010**, 132, 9843-9849.
- Desu, S. B.; Obryan, H. M., *J. Am. Ceram. Soc.* **1985**, 68, 546-551.
- Hughes, H.; Iddles, D. M.; Reaney, I. M., *Appl. Phys. Lett.* **2001**, 79, 2952-2954.
- Mallinson, P. M.; Claridge, J. B.; Rosseinsky, M. J.; Ibberson, R. M.; Wright, J. P.; Fitch, A. N.; Price, T.; Iddles, D. M., *Appl. Phys. Lett.* **2007**, 91, 222901.
- Bieringer, M.; Moussa, S. M.; Noailles, L. D.; Burrows, A.; Kiely, C. J.; Rosseinsky, M. J.; Ibberson, R. M., *Chem. Mater.* **2003**, 15, 586-597.
- Surendran, K. P.; Sebastian, M. T.; Mohanan, P.; Moreira, R. L.; Dias, A., *Chem. Mater.* **2005**, 17, 142-151.
- Thirumal, M.; Davies, P. K., *J. Am. Ceram. Soc.* **2005**, 88, 2126-2128.

18. Moussa, S. M.; Claridge, J. B.; Rosseinsky, M. J.; Clarke, S.; Ibberson, R. M.; Price, T.; Iddles, D. M.; Sinclair, D. C., *Appl. Phys. Lett.* **2003**, *82*, 4537-4539.
19. Mallinson, P.; Claridge, J. B.; Iddles, D.; Price, T.; Ibberson, R. M.; Allix, M.; Rosseinsky, M. J., *Chem. Mater.* **2006**, *18*, 6227-6238.
20. Kan, A.; Ogawa, H.; Yokoi, A.; Ohsato, H., *Jpn. J. Appl. Phys.* **2006**, *45*, 7494-7498.
21. Cao, J.; Kuang, X.; Allix, M.; Dickinson, C.; Claridge, J. B.; Rosseinsky, M. J.; Iddles, D. M.; Su, Q., *Chem. Mater.* **2011**, *23*, 5058-5067.
22. Collins, B. M.; Jacobson, A. J.; Fender, B. E. F., *J. Solid State Chem.* **1974**, *10*, 29-35.
23. Fang, L.; Li, C. C.; Peng, X. Y.; Hu, C. Z.; Wu, B. L.; Zhou, H. F., *J. Am. Ceram. Soc.* **2010**, *93*, 1229-1231.
24. Hughes, H.; Azough, F.; Freer, R.; Iddles, D., *J. Eur. Ceram. Soc.* **2005**, *25*, 2755-2758.
25. Suresh, M. K.; John, A.; Thomas, J. K.; Wariar, P. R. S.; Solomon, S., *Mater. Res. Bull.* **2010**, *45*, 1389-1395.
26. Teneze, N.; Boullay, P.; Petricek, V.; Trolliard, G.; Mercurio, D., *Solid State Sci.* **2002**, *4*, 1129-1136.
27. Rietveld, H. M., *J. Appl. Crystallogr.* **1969**, *2*, 65-71.
28. Coelho, A. A. *TOPAS Academic V4*, Coelho Software: Brisbane, Australia, 2005.
29. Brown, I. D.; Altermatt, D., *Acta Crystallogr., Sect. B* **1985**, *41*, 244-247.
30. Hakki, B. W.; Coleman, P. D., *IEEE Trans. Microwave Theory Tech.* **1960**, *8*, 402-410.
31. Lufaso, M. W.; Hopkins, E.; Bell, S. M.; Llobet, A., *Chem. Mater.* **2005**, *17*, 4250-4255.
32. Evans, I. R.; Howard, J. A. K.; Evans, J. S. O., *J. Mater. Chem.* **2003**, *13*, 2098-2103.
33. Sears, V. F., *Neutron News* **1992**, *3*, 26-37.
34. Irvine, J. T. S.; Sinclair, D. C.; West, A. R., *Adv. Mater.* **1990**, *2*, 132-138.
35. Thirumal, M.; Davies, P. K., *J. Mater. Sci.* **2011**, *46*, 4715-4718.
36. Rawal, R.; Feteira, A.; Flores, A. A.; Hyatt, N. C.; West, A. R.; Sinclair, D. C.; Sarma, K.; Alford, N. M., *J. Am. Ceram. Soc.* **2006**, *89*, 336-339.
37. Yu, X.; Chai, S.; Kuang, X.; Su, C.; Pan, F.; Fang, L.; Su, Q., *J. Am. Ceram. Soc.* **2013**, *96*, 2510-2514.
38. Trolliard, G.; Teneze, N.; Boullay, P.; Mercurio, D., *J. Solid State Chem.* **2004**, *177*, 1188-1196.
39. Goodenough, J. B.; Kafalas, J. A., *J. Solid State Chem.* **1973**, *6*, 493-501.
40. Mizoguchi, H.; Woodward, P. M.; Byeon, S. H.; Parise, J. B., *J. Am. Ceram. Soc.* **2004**, *126*, 3175-3184.
41. Eng, H. W.; Barnes, P. W.; Auer, B. M.; Woodward, P. M., *J. Solid State Chem.* **2003**, *175*, 94-109.
42. Lufaso, M. W.; Woodward, P. M., *Acta Crystallogr. Sect. B* **2004**, *60*, 10-20.
43. Wheeler, R. A.; Whangbo, M. H.; Hughbanks, T.; Hoffmann, R.; Burdett, J. K.; Albright, T. A., *J. Am. Chem. Soc.* **1986**, *108*, 2222-2236.
44. Zhurova, E. A.; Ivanov, Y.; Zavodnik, V.; Tsirelson, V., *Acta Crystallogr. Sect. B* **2000**, *56*, 594-600.
45. Kennedy, B. J.; Prodjosantoso, A. K.; Howard, C. J., *J. Phys.: Condens. Matter* **1999**, *11*, 6319-6327.
46. Hewat, A. W., *J. Phys. C: Solid State Phys.* **1973**, *6*, 2559.
47. Kuang, X.; Allix, M. M. B.; Claridge, J. B.; Niu, H. J.; Rosseinsky, M. J.; Ibberson, R. M.; Iddles, D. M., *J. Mater. Chem.* **2006**, *16*, 1038-1045.
48. Lu, F.; Kuang, X., *J. Solid State Chem.* **2015**, *221*, 152-157.
49. De Paoli, J. M.; Alonso, J. A.; Carbonio, R. E., *J. Phys. Chem. Solids* **2006**, *67*, 1558-1566.
50. Rawal, R.; McQueen, A. J.; Gillie, L. J.; Hyatt, N. C.; McCabe, E. E.; Samara, K.; Alford, N. M.; Feteira, A.; Reaney, I. M.; Sinclair, D. C., *Appl. Phys. Lett.* **2009**, *94*, 192904.
51. Waburg, M.; Müller-Buschbaum, H., *Monatsh. Chem.* **1984**, *115*, 15-20.
52. Mössner, B.; Kemmler-Sack, S., *J. Less-Common Met.* **1986**, *120*, 287-291.
53. Van Duivenboden, H. C.; Zandbergen, H. W.; Ijdo, D. J. W., *Acta Crystallogr. Sect. C* **1986**, *42*, 266-268.
54. Rother, H. J.; Kemmler-Sack, S.; Treiber, U.; Cyris, W. R., *Z. Anorg. Allg. Chem.* **1980**, *466*, 131-138.
55. Abakumov, A. M.; Tendeloo, G. V.; Scheglov, A. A.; Shpanchenko, R. V.; Antipov, E. V., *J. Solid State Chem.* **1996**, *125*, 102-107.
56. Ling, C. D.; Avdeev, M.; Kharton, V. V.; Yaremchenko, A. A.; Macquart, R. B.; Hoelzel, M., *Chem. Mater.* **2010**, *22*, 532-540.
57. Bertaut, E. F.; Corliss, L.; Forrat, F.; Aleonard, R.; Pauthenet, R., *J. Phys. Chem. Solids* **1961**, *21*, 234-251.
58. Kumada, N.; Taki, K.; Kinomura, N., *Mater. Res. Bull.* **2000**, *35*, 1017-1021.
59. Blasse, G., *J. Inorg. Nucl. Chem.* **1964**, *26*, 1191-1199.